CHEMISTRY OF MATERIALS
Article

*Chem. Mater.* **2011,** *23,* 85–94 85
DOI:10.1021/cm102483m

# Substitution Effect on the Interplane Coupling in Crednerite: the $Cu_{1.04}Mn_{0.96}O_2$ Case

M. Poienar,*,† C. Vecchini,‡,§ G. André,∥ A. Daoud-Aladine,‡ I. Margiolaki,⊥ A. Maignan,† A. Lappas,§ L. Chapon,‡ M. Hervieu,† F. Damay,∥ and C. Martin†

†*Laboratoire CRISMAT, CNRS UMR 6508, 6 Bd Ml Juin, 14050 CAEN CEDEX, France,* ‡*ISIS Facility, Rutherford Appleton Laboratory-STFC, Chilton, Didcot, Oxfordshire OX11 0QX, United Kingdom,* §*Institute of Electronic Structure and Laser, Foundation for Research and Technology−Hellas, Vassilika Vouton, 711 10 Heraklion, Crete, Greece,* ∥*Laboratoire Léon Brillouin, CEA-CNRS UMR 12, 91191 GIF-SUR-YVETTE CEDEX, France, and* ⊥*ESRF- Polygone Scientifique Louis Néel -6, rue Jules Horowitz, 38000 Grenoble, France*

*Received August 30, 2010. Revised Manuscript Received November 19, 2010*

The 4%Cu for Mn substitution in $CuMnO_2$ decreases slightly the lattice parameters, reduces the Jahn−Teller distortion of the $MnO_6$ octahedra, but does not change the temperature dependence of the structure, showing a $C2/m$ to $P\bar{1}$ structural transition (in the vicinity of the magnetic transition temperature). In contrast, the antiferromagnetic structure is strongly modified by the substitution, as a propagation vector $\mathbf{k} = (0\ ^1/_2\ 0)$ is evidenced for $Cu_{1.04}Mn_{0.96}O_2$ compared to $\mathbf{k} = (0\ ^1/_2\ ^1/_2)$ for $CuMnO_2$. Consequently, the interplane magnetic coupling (along the $c$ axis) changes from antiferromagnetic in $CuMnO_2$ to ferromagnetic in $Cu_{1.04}Mn_{0.96}O_2$ without change in the antiferromagnetic arrangement of the ferromagnetic chains in the $(a,b)$ plane. The nanostructural study points toward the existence of numerous defects at the nanoscale which justify the modeling of strains used in the refinement of the crystalline structure.

## Introduction

Recently, the $ABO_2$ delafossite-type class of materials, B being a transition element, has attracted a lot of interest. On the one hand, in the field of transparent conducting oxides, thin films of $CuAlO_2$ show the unusual combination of high transparency and rather high p-type semiconductivity.[1] On the other hand, in the field of exotic magnetic and structural properties, delafossite $CuFeO_2$ is a complex example of a triangular lattice antiferromagnet, extensively studied over the past years for its multiferroicity.[2,3]

Comparatively, the magnetic interactions and coupling in $AMnO_2$ antiferromagnets, with A = Cu or Na have been less studied.[4,5] They are also layered compounds like those crystallizing with the rhombohedral delafossite structure, but the Jahn−Teller distortion of the $Mn^{3+}$ octahedral environment lowers the trigonal symmetry to monoclinic ($C2/m$). As a result, one of the main differences between delafossite and crednerite compounds lies in the topology of the planar triangular lattice, which leads to isotropic in-plane magnetic interactions ($J_1$) in the former case, but to anisotropic interactions ($J_1$, $J_2$) in the latter. For both structures, the out-of-plane magnetic exchanges have also to be taken in consideration to explain the magnetic ordering that is associated with a strong magneto-elastic coupling in $CuMnO_2$,[6] and $NaMnO_2$.[5]

Magnetic lattice dilution is in itself a vast field of challenging new physics. A good illustration is the drastic effect of a small level of substitution upon the magnetic structure of $CuFeO_2$ which changes from collinear to helical.[7−10] Moreover, it is well-known that, in other magnetic oxides such as manganese perovskites, small deviations from the stoichiometry or small substitutions can induce a wide variety of changes, such as a change from an antiferromagnetic to a ferromagnetic structure.[11,12]

Keeping in mind these trends and the possibility to substitute Cu for Mn, according to the $Cu_{1+x}Mn_{1-x}O_2$ solid

*To whom correspondence should be addressed. E-mail: maria.poienar@ensicaen.fr.

(1) Kawazoe, H.; Yasukawa, M.; Hyodo, H.; Kurita, M.; Yanagi, H.; Hosono, H. *Nature* (*London*) **1997**, *389*, 939.
(2) Kimura, T.; Lashley, J. C.; Ramirez, A. P. *Phys. Rev. B* **2006**, *73*, 220401.
(3) Ye, F.; Ren, Y.; Huang, Q.; Fernandez-Baca, J. A.; Dai, P. C.; Lynn, J. W.; Kimura, T. *Phys. Rev. B* **2006**, *73*, 220404.
(4) Doumerc, J. P.; Trari, M.; Topfer, J.; Fournes, L.; Grenier, J. C.; Pouchard, M.; Hagenmuller, P. *Europ. J. Solid State Inorg. Chem.* **1994**, *31*, 705.
(5) Giot, M.; Chapon, L. C.; Androulakis, J.; Green, M. A.; Radaelli, P. G.; Lappas, A. *Phys. Rev. Lett.* **2007**, *99*, 247211.
(6) Damay, F.; Poienar, M.; Martin, C.; Maignan, A.; Rodriguez-Carvajal, J.; André, G.; Doumerc, J. P. *Phys. Rev. B* **2009**, *80*, 094410.
(7) Terada, N.; Mitsuda, S.; Suzuki, S.; Kawasaki, T.; Fukuda, M.; Nagao, T.; Katori, H. A. *J. Phys. Soc. Jpn.* **2004**, *73*, 1442–1445.
(8) Nakajima, T.; Mitsuda, S.; Takhashi, M.; Yamano, M.; Masuda, K.; Yamazaki, H.; Prokes, K.; Kiefer, K.; Gerischer, S.; Terada, N.; Kitazawa, H.; Kimura, H.; Noda, Y.; Soda, M.; Matsuura, M.; Hirota, K. *Phys. Rev. B* **2009**, *79*, 214423.
(9) Seki, S.; Yamasaki, Y.; Shiomi, Y.; Iguchi, S.; Onose, Y.; Tokura, Y. *Phys. Rev. B* **2007**, *75*, 100403.
(10) Terada, N.; Nakajima, T.; Mitsuda, S.; Kitazawa, H.; Kaneko, K.; Metoki, N. *Phys. Rev. B* **2008**, *78*, 014101.
(11) Maignan, A.; Martin, C.; Raveau, B. *Z. Phys. B* **1997**, *102*, 19–24.
(12) Damay, F.; Martin, C.; Maignan, A.; Hervieu, M.; Raveau, B.; Bourée, F.; André, G. *Appl. Phys. Lett.* **1998**, *73*, 3772–3774.

© 2010 American Chemical Society
Published on Web 12/13/2010

solution,[13,14] a reinvestigation of this crednerite system was undertaken. In this paper, we report on the results of the structural and magnetic studies of $Cu_{1.04}Mn_{0.96}O_2$, characterized by X-ray and neutron powder diffraction, in addition to transmission electron microscopy observations. It is shown that, remarkably, this substitution affects mainly the interplane coupling from antiferromagnetic in $CuMnO_2$[6] to ferromagnetic for $Cu_{1.04}Mn_{0.96}O_2$. In contrast, the intraplane couplings, or the frustration-lifting mechanism, are only slightly affected, though the substitution is made at the level of the $MnO_2$ layers. The structural defects observed by electron microscopy explain why strain parameters have to be used in structural refinements and give arguments to discuss the magnetic behavior.

## Experimental Section

A polycrystalline sample (10 g) of $Cu_{1.04}Mn_{0.96}O_2$ was prepared by solid state reaction in an evacuated silica tube. Powders of CuO and MnO were weighted according to the 1.04 CuO:0.96 MnO stoichiometric ratio, carefully crushed, sieved, and then pressed in the form of a rod (6 mm diameter and several cm length). The rod was then placed in an alumina crucible, introduced in an evacuated silica tube, and heated at 950 °C for 12 h.

The quality of the compound was checked by room temperature (RT) X-ray powder diffraction (XRPD), using a Panalytical Xpert Pro diffractometer, with $CuK_\alpha$ radiations. The XRPD pattern was refined using the Fullprof Suite,[15] showing that the sample is well crystallized and single phase with the expected crednerite-type structure.

The nanostructural study was carried out by transmission electron microscopy (TEM). A small amount of sample was crushed in an agate mortar containing *n*-butanol, and the flakes were deposited on an aluminum grid covered with a holey carbon film. The electron diffraction (ED) investigation was carried out with a JEOL 200 CX microscope. The microscope used for high-resolution transmission electron microscopy (HRTEM) was a TOPCON operating at 200 kV, with a spherical aberration coefficient Cs = 0.4 mm. Both microscopes are equipped with energy dispersive spectroscopy (EDS) QUEVEX analyzers. HRTEM images were simulated using the Mac Tempas software and the positional parameters obtained from the herein structural refinements.

High resolution X-ray diffraction patterns were recorded on ID31 beamline, at the ESRF ($\lambda$ = 0.399856 Å). The sample was mounted in a cryostat in a 0.8 mm capillary, and the scans were performed in a $2\theta$ angle from 0.3° to 43°; eleven measurements were performed in the 20−90 K range, and one pattern was taken at 290 K. Seven sets of time-of-flight neutron powder diffraction data were collected on HRPD at the ISIS facility between 5 and 75 K and one at $T$ = 270 K. Neutron powder diffraction (NPD) versus temperature was performed on the G4.1 diffractometer ($\lambda$ = 2.428 Å) at LLB from 1.5 to 105 K by a 10 K step and up to 135 K by 5 K steps. Symmetry analysis for the magnetic phase transitions was performed using the BasIreps program, part of the FullProf Suite, as well as programs available on the Bilbao Crystallographic Server.[16,17]

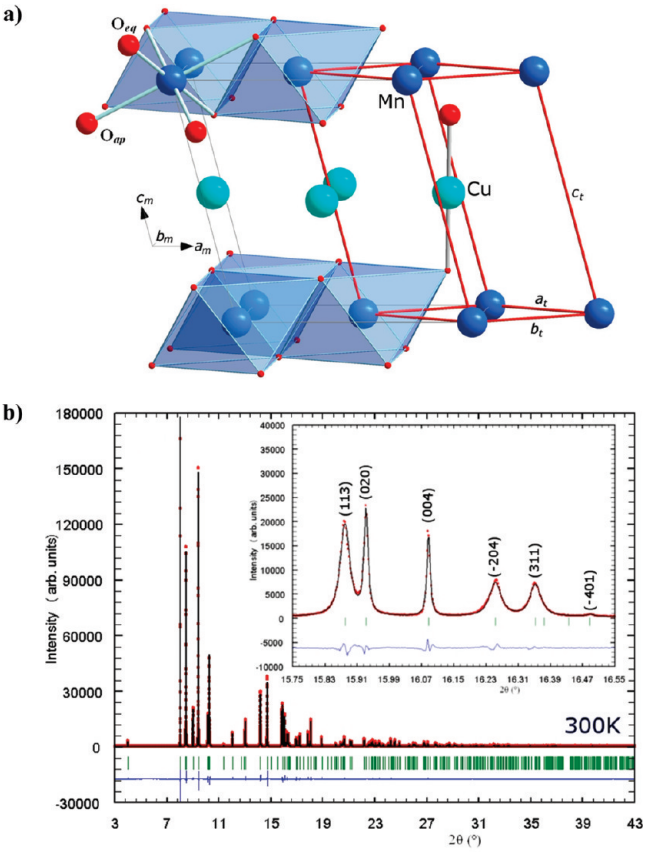


**Figure 1.** (a) Relationship between the room temperature monoclinic $C2/m$ ($a_m$, $b_m$, $c_m$) structure and the low temperature triclinic cell $P\bar{1}$ ($a_t$, $b_t$, $c_t$), outlined in red. (b) Rietveld refinement of the room temperature synchrotron X-ray powder diffraction data of $Cu_{1.04}Mn_{0.96}O_2$. Experimental data are represented by open circles, the calculated profile by a continuous line, and the allowed structural Bragg reflections by vertical marks. The difference between the experimental and calculated profiles is displayed at the bottom of the graph. Inset: detail of the refined and experimental profiles.

## Results

**1. Room Temperature Crystal Structure.** The results of the refinements of RT synchrotron X-ray and neutron diffraction data are in agreement with those previously reported on single-crystals[14] of $Cu_{1.04}Mn_{0.96}O_2$ and close to those obtained for poly crystals of $CuMnO_2$.[6,18] The system crystallizes in the $C2/m$ space group with $a_m$ = 5.5754(3) Å, $b_m$ = 2.8847(1) Å, $c_m$ = 5.8941(3) Å, and $\beta_m$ = 104.244(1)°; see structure in Figure 1 (where *m* and *t* labels are used for monoclinic and triclinic structures, respectively, to help the reading). To facilitate the reading, the "esd" (estimated standard deviation) values, dealing with interatomic distances reported in Table 1 and 3, are dropped in the text.

The coupled selected area electron diffraction (SAED) and EDS analyses were carried out to check the crystallinity and homogeneity of the sample. The reconstruction

(13) Trari, M.; Topfer, J.; Dordor, P.; Grenier, J. C.; Pouchard, M.; Doumerc, J. P. *J. Solid State Chem.* **2005**, *178*, 2751–2758.
(14) Topfer, J.; Trari, M.; Gravereau, P.; Chaminade, J. P.; Doumerc, J. P. *Z. Kristallogr.* **1995**, *210*, 184.
(15) Rodriguez-Carvajal, J. *Physica B* **1993**, *192*, 55.
(16) Aroyo, M. I.; Perez-Mato, J. M.; Capillas, C.; Kroumova, E.; Ivantchev, S.; Madariaga, G.; Kirov, A.; Wondratschek, H. *Z. Kristallogr.* **2006**, *221*, 15.
(17) Aroyo, M. I.; Kirov, A.; Capillas, C.; Perez-Mato, J. M.; Wondratschek, H. *Acta Crystallogr., Sect. A* **2006**, *62*, 115.
(18) Kondrashev, I. D. *Soviet Phys. Crystallogr.* **1959**, *3*, 703.

**Table 1. (a) Room Temperature Crystallographic Parameters, Refined from HRPD, and (b) Corresponding Inter-Atomic Distances (Å), with Multiplicity, and Angles (deg)**

(a) Room Temperature Crystallographic Parameters, Refined from HRPD

| | bank1 | bank2 |
|---|---|---|
| *C2/m* (no. 12)<br>$a_m$ = 5.5754(3) Å<br>$b_m$ = 2.8847(1) Å<br>$c_m$ = 5.8941(3) Å<br>$\beta_m$ = 104.244(1)°<br>$V$ = 91.887(1) Å$^3$ | $R_{Bragg}$ = 2.89%<br>$R_F$ = 2.66%<br>$\chi^2$ = 1.92 | $R_{Bragg}$ = 1.02%<br>$R_F$ = 1.61%<br>$\chi^2$ = 6.80 |

| atom | Wyckoff site | $x$ | $y$ | $z$ | occupation |
|---|---|---|---|---|---|
| Cu | (2d) | 0 | 0.5 | 0.5 | 1.0042 |
| Mn,Cu | (2a) | 0 | 0 | 0 | 0.960(2),0.040 |
| O | (4i) | 0.4073(5) | 0 | 0.1789(4) | 2 |

anisotropic factors ($\times 10^4$)

| atom | $\beta_{11}$ | $\beta_{22}$ | $\beta_{33}$ | $\beta_{13}$ |
|---|---|---|---|---|
| Cu | 127(2) | 253(5) | 40(2) | 20(1) |
| Mn, Cu | 55(3) | 90(10) | 30(3) | 17(2) |
| O | 91(2) | 128(5) | 31(1) | 21(1) |

(b) Corresponding Inter-Atomic Distances (Å), with Multiplicity, and Angles (deg)

| | | | |
|---|---|---|---|
| Cu−O | 1.8347(2) (×2) | $O_{eq}$−Mn−$O_{eq}$ | 96.671(8) |
| Mn−$O_{eq}$ | 1.9308(2) (×4) | | |
| | | $O_{ap}$−Mn−$O_{eq}$ | 96.796(17) |
| Mn−$O_{ap}$ | 2.2567(3) (×2) | | |
| | | Mn−O−Mn | 96.671(8) |
| | | | 96.796(8) |
| Mn−Mn | 2.8848(3) | | |
| Mn−Mn | 3.1388(3) (×2) | | |

of the reciprocal space confirmed the above parameters and space group. The [110] and [010] electron diffraction patterns are given in Figure 2. The EDS analyses carried out on more than hundred crystallites evidenced the cationic homogeneity of the sample within the experimental errors and the absence of manganese oxides as secondary phase.

The crystallographic parameters obtained from the refinement of high-resolution neutron powder diffraction data are given in Table 1. The structure can be described as a stacking of layers made of edge sharing $MnO_6$ octahedra and of oxygen free Cu sheets, the copper ions are linearly coordinated by two oxygen ions, forming O−Cu−O "dumbbells" perpendicularly to the (*a, b*) plane (Figure 1a). The $MnO_6$ octahedra are elongated with four short equatorial (1.9308 Å) and two long apical (2.2567 Å) Mn−O distances, which lead to a ferro-orbital ordering of the $d_{z^2}$ orbitals in the (*a, c*) plane. In the (*a, b*) plane, the Mn cations form an anisotropic triangular network with one short and two long Mn−Mn distances (2.8848 and 3.1388 Å, corresponding to $J_1$ and $J_2$, respectively), which differs from the regular triangular network characteristic of delafossite.

From NPD data, the oxygen content is refined to 2.00(1) per $ABO_2$ unit, and the occupancy of the (2a) site leads to 0.960(2) Mn for 0.040 Cu; that is the expected composition. To respect the electrical neutrality, since neither oxygen vacancies nor extra oxygen in the Cu layer have been found, and considering that copper on the manganese site is either trivalent or divalent, two limit formulas are obtained, $[Cu^+][Cu^{3+}_{0.04}Mn^{3+}_{0.96}]O_2$ and $[Cu^+][Cu^{2+}_{0.04}Mn^{3+}_{0.92}Mn^{4+}_{0.04}]O_2$, respectively.

The cell volume of $Cu_{1.04}Mn_{0.96}O_2$ is smaller than the one of $CuMnO_2$ (91.887 Å$^3$ and 92.167 Å$^3$, respectively); it corresponds mainly to a decrease of *a*, an important increase of the $\beta$ angle, and a very small increase of *c*. The changes in the $\beta$ angle and *a* parameter will have effects on the exchange interactions between the (*a, b*) planes and in the basal plane, respectively. In the same way, the dilution on the Mn site, because of the small substitution of Cu for Mn, induces a smaller ⟨Mn−O⟩ average distance (2.0394(3) Å compared to 2.0424(5) Å for $CuMnO_2$) and a slightly smaller Jahn−Teller distortion of the $MnO_6$ octahedra (by comparing the $\delta = d(Mn-O)_{apical}/d(Mn-O)_{equatorial}$). The triangular Mn lattice in the basal plane is also more regular with the shortest Mn−Mn distance (2.8848 Å) slightly longer than in $CuMnO_2$ (2.8822 Å) and, concomitantly the two longest distances (3.1388 Å) smaller than in $CuMnO_2$ (3.1468 Å). At room temperature, the Cu−O distance is almost unaffected by the substitution, close to 1.8369 Å in $CuMnO_2$ and to 1.8347 Å in $Cu_{1.04}Mn_{0.96}O_2$. The values of the anisotropic displacement factors (Table 1) show that, as expected, the largest values are for Cu, with $\beta_{11}$ ($\beta_{22}$) $\gg \beta_{33}$ corresponding to flattened ellipsoids along the *c* axis. This is often encountered in such layered structures with O−Cu−O dumbbell perpendicular to the (*a, b*) plane, and can be explained by the "guitar string" transversal vibrational modes.[19]

During the refinements, it has been necessary to introduce a strain model characteristic of the monoclinic Laue class, to account for the (*h k l*) dependent broadening of Bragg peaks (inset Figure 1b); the quality of the corresponding refinement is illustrated in Figure 1b.[20,21] The values of the Stephens strain parameters are reported in Table 2, along with the ones obtained for $CuMnO_2$, showing that the substitution favors strains, the values being higher in each crystallographic direction. It is thus reasonable to attribute the strains to the local disorder induced by cations of different sizes and electronic configurations at the same crystallographic site.

To understand the origins of these strain phenomena, the nanostructural state has been studied using transmission electron microscopy. More or less intense additional spots are often observed in the electron diffraction patterns, resulting from the presence of twinning domains and misoriented zones in the crystallites, and could get to the formation of concentric partial rings, close to Debye−Scherrer diagrams. Bright and dark field images of almost all the crystallites show an inhomogeneous contrast; whatever the orientation, bright and darker zones are observed at a scale of a few tens of a nanometer. These local modulations of the contrast are the signatures of

(19) Evans, J. S. O. *J. Chem. Soc., Dalton Trans.* **1999**, 3317–3326.
(20) Rodriguez-Carvajal, J.; Fernandez-Diaz, M. T.; Martinez, J. L. *J. Phys.: Condens. Matter* **1991**, *3*, 3215.
(21) Stephens, P. W. *J. Appl. Crystallogr.* **1999**, *32*, 281.

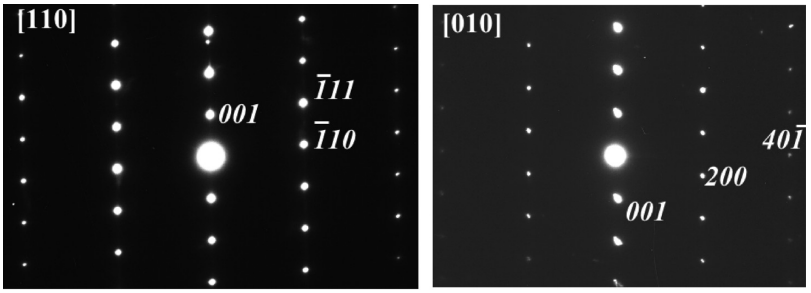


**Figure 2.** (a) [110] and (b) [010] SAED patterns of $Cu_{1.04}Mn_{0.96}O_2$.

**Table 2. Refined Strain Parameters of $Cu_{1.04}Mn_{0.96}O_2$ and $CuMnO_2$ from RT HRPD Data**

| $S_{400}$ | $S_{040}$ | $S_{220}$ | $S_{202}$ | $S_{022}$ | $S_{121}$ | $S_{301}$ |
|---|---|---|---|---|---|---|
| | | | $Cu_{1.04}Mn_{0.96}O_2$ | | | |
| 0.74(3) | 1.29(9) | 2.9(2) | 4.18(9) | 7.3 (2) | 5.1(5) | 2.2(1) |
| | | | $CuMnO_2$ | | | |
| 0.22(2) | 0.17(5) | 0.7(1) | 1.48(7) | 1.8(1) | 1.6(2) | 0.67(6) |

intensive strain fields, which result from misfit accommodations through different zones of the crystallites.

A first example of twinning domains is illustrated by the [110] ED pattern in Figure 3a, where the spot spacing is doubled in one row parallel to $\vec{c}^*$ out of two. Such patterns, which are systematically observed, are easily explained by the fact that the (−130) planes play the role of mirror. The corresponding bright field images (not presented herein) show that the twinning domains are large, up to several hundred nanometers and exhibit coherent twin boundaries (TB) as schematically drawn in Figure 3c. Note that such TBs involve a slight puckering of the (*a,b*) layers. The average width of these domains suggests that they are not responsible of the strain phenomena.

A second example of multiple systems in ED patterns is given in Figure 3b, where the system of intense spots is associated to the [010] zone axis (white numbers). The second system exhibits a distorted pseudo hexagonal arrangement (spots circled in pink) with a doubling of the periodicities along two directions (see pink arrows). The $d_{hkl}$ distances and angles measurements show that they do not fit exactly with any of the possible zone axes considering the *C*2/*m* monoclinic phase but is reminiscent of the [001] pattern. This second system is indexed with $a_s$ close but different of $b_s \approx 6.2$ Å and $\gamma_s \approx 57°$ (s is the subscript for superstructure in Figure 3b). The geometrical relationships between the two adjacent domains and their relative orientations are given in Figure 4b. The TEM images show that the corresponding domains are small, average widths being of the order of a few nanometers, and coexist with other differently oriented domains; as a consequence the reciprocal space could not be reconstituted by tilting. One of these HRTEM images is given in Figure 4a, with the inserted Fast Fourier Transforms (FFT). The left part of the image corresponds to a [010] zone axis, where the bright dots are correlated to the cationic positions, with the brighter dots associated to the Cu positions and the less bright to the Mn ones. The simulated image, calculated for a focus value close to −500 Å and a crystal thickness of 35 Å is superposed; the atomic numbers of Cu and Mn being close, the difference in contrast is correlated to the oxygen environments of each cation. In the right part of the image, the FFT evidence a pattern similar to the pattern of the supercell. The contrast consists in a pseudo hexagonal arrangement of bright dots, about 6 Å spaced. The domain boundary (DB) is parallel to (001) of the *C*2/*m* phase, and the twin interface at the level of one (001) manganese layer with the variation of contrast of one bright dot out of two. The amplitude of the brightness variation implies a rather significant atomic rearrangement. Considering these observations without knowing the exact nature of this cell, several models could be proposed including one with ordered manganese vacancies forming Kagome-like (001) layers. In the *C*2/*m*-type domain, one defect is observed in the thin part of the crystal (indicated by a large arrow): one additional row of gray dots is inserted between two rows of bright dots. This defect can be explained by the stacking, along the *c* axis, of two compact octahedral layers sandwiched between two copper layers; this defect involves the formation of an antiphase boundary (AB) through the connection of Mn and Cu (*a, b*) layers, along the *a* axis, as schematically drawn in Figure 4c.

Figure 5a is a typical [001] HRTEM image of a grainy microstructure of the *C*2/*m* phase, with maxima and minima of brightness, used to highlight the structural phenomena at the origin of the strain, by describing three types of contrasts (labeled 1 to 3 in this image). The center of the enlarged zone numbered ① (Figure 5b) does not show any strain as evidenced by the FFT characterized by sharp spots (see the circled 020 and 200 reflections) and symmetric pattern. The contrast consists in staggered rows of bright (Cu positions) and less bright (Mn positions) dots running along *b*; the simulated image (focus −500 Å and thickness close to 35 Å) is superposed. The contrast progressively changes going toward the right upper corner, where the FFT shows a splitting of the reflections in two elongated spots (enlarged 020 reflection in inset), as a consequence of the zone axis evolution associated to a local distortion. In the zone numbered ② (Figure 5c), the reflections are split in four spots (enlarged 200 reflection in inset) indicating slight misorientations and amplitude variations of the corresponding vectors. The HRTEM images show that they

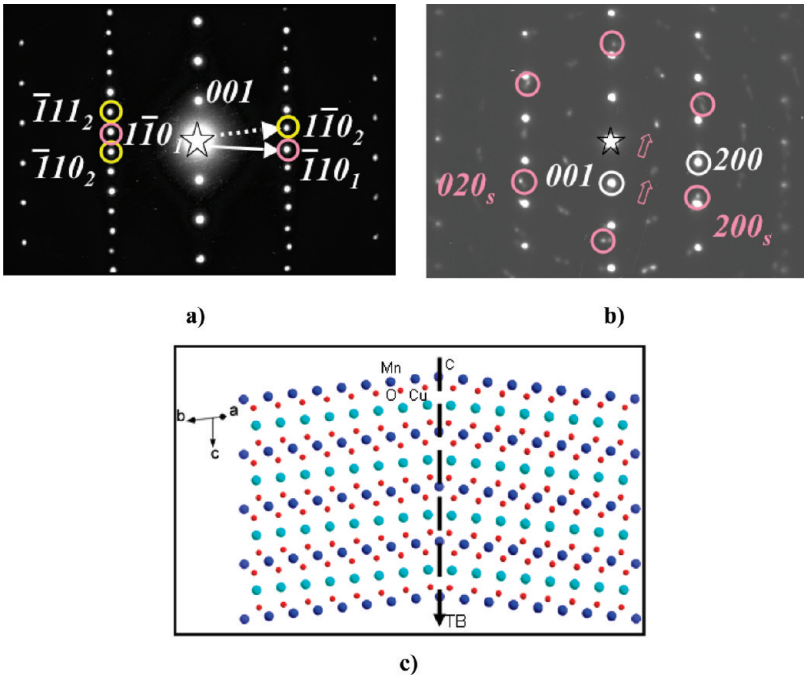


**Figure 3.** (a) [110] ED pattern typical of twinning domains; pink and yellow circles are used for indexing the two variants. (b) Example of multiple systems in ED patterns: white indices are associated to a [010] zone axis of the *C2/m* phase and the pink ones to a [001] zone axis of a supercell; (c) idealized model of the twin domains.

are the result of the formation of dislocations and antiphase boundaries. The dislocations can be observed by viewing at grazing incidence, three of them being outlined by arrows following the atomic rows along the *b* axis: three rows linked to only two rows. These dislocations can be accommodated, as usual, by a rather intense bending of the adjacent atomic rows (see the large arrow) or by the propagation of an antiphase boundary (AB, shown by a dotted line) along different directions depending on the local rearrangement and associated to a shift $\vec{t} \approx 1/4\vec{a}$ of the atomic rows. Models of these defective zones, with dislocation, antiphase boundary, and row bending are schematically drawn in Figure 5d; the triangles materialize the upper faces of the octahedra, and the yellow atoms represent the defective cationic positions which could be occupied by Mn, Cu, or be vacant. Lastly, in the thicker zone labeled ③, the formation of all these local distortions generate Moiré patterns.

As a conclusion of the microstructural study, whatever the zone axis, the images evidence important strain fields with the formation of differently oriented domains, from large twinning domains resulting from the existence of mirror planes down to slight misorientation of nanometric scaled areas. All the observed phenomena (from simple row bending up to dislocation, AB, and likely superstructures) appear as different ways to accommodate the differences in the lattice parameters of the differently oriented domains. The larger difference between the *a* and *c*-cell parameters in $Cu_{1.04}Mn_{0.96}O_2$ than in $CuMnO_2$ is thus in agreement with the larger strain parameters refined for the former (Table 2). Moreover, the presence of cations of different sizes and electronic configurations on the same crystallographic site could favor the local disorder and such structural rearrangements. This need of accommodation could be explained by the existence, at high temperature, of a more symmetric structure with the same structural type, not necessary rhombohedral as the delafossite-type structure but at least hexagonal considering the layers' stacking mode.

All these observations of misoriented nanodomains and their accommodation are consistent with the synchrotron X-ray and neutron diffraction data: they support the use of strain parameters to refine the structure. Furthermore, these perturbations of the lattice have probably some effects upon the magnetism, particularly on the domain formation.

**2. Evolution of the Crystal and Magnetic Structures at Low Temperature.** In $Cu_{1.04}Mn_{0.96}O_2$, an antiferromagnetic transition is observed at about 60 K, and as in the case of $CuMnO_2$,[6] a lowering of symmetry from a monoclinic to a triclinic cell is also observed (Figure 6). The corresponding *C2/m* to $P\bar{1}$ structural transition is evidenced in the high resolution synchrotron X-ray and high resolution neutrons (not shown) diffraction pattern by a broadening of numerous peaks when a temperature around 50 K is reached, followed by clear peaks splitting below 45 K (shown at 20 K in Figure 7). The symmetry lowering appears therefore as a consequence of the magnetic transition.

The refinement of the 5 K time-of-flight neutron diffraction data leads to a triclinic structure, $P\bar{1}$ space group, with $a_t = 3.1341(4)$ Å, $b_t = 3.1275(4)$ Å, $c_t = 5.8935(5)$ Å, $\alpha_t = 102.54(1)°$, $\beta_t = 102.64(1)°$, and $\gamma_t = 54.784(4)°$. In this low temperature structure, the three angles $\alpha_t$, $\beta_t$, and $\gamma_t$ have to be refined, while the oxygen atoms occupy a general symmetry lattice site (*x*, *y*, *z*) (Table 3) and the relation between the monoclinic (labeled *m*) and triclinic (*t*) structures is given in Figure 1a. Isotropic displacement factors were used to limit the number of independent parameters in the refinement, and a triclinic class strain model was applied.

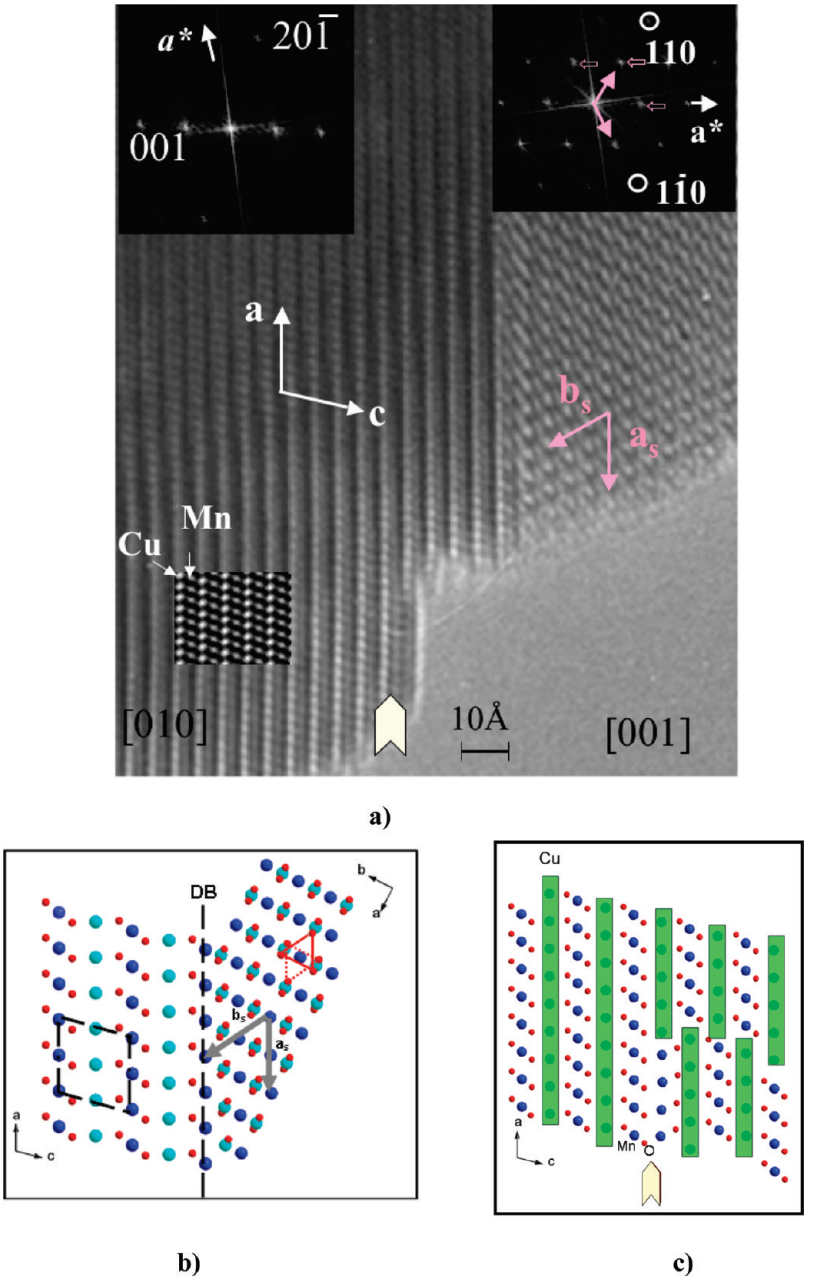


**Figure 4.** (a) [010] HRTEM image associated to a SAED pattern similar to that of Figure 3b and FFT and simulated image in insets. The bright dots are correlated to the cationic positions. One area of the superstructure is observed in the right part of the image. The large arrow indicates a layer stacking defect and the resulting antiphase boundary. (b and c) Idealized models of the domain boundary (DB) and layer stacking defect, respectively.

Dealing with the triangular Mn-array in the ($a$, $b$) plane, the Mn−Mn shortest edge of the triangle is slightly compressed (from 2.8848 Å along $[010]_m$ to 2.8809 Å along $[1\bar{1}0]_t$) and the two equal longer Mn−Mn distances (3.1388 Å at RT) become non-equivalent with a larger contraction along $b_t$ (3.1276 Å) than that along $a_t$ (3.1341 Å) (Figure 6a). In the $MnO_6$ octahedron, the two long apical Mn−O distances decrease from 2.2567 Å at RT to 2.2488 Å, while the four equatorial distances (1.9308 Å at RT) are now separated in two subsets, a slightly shortened (1.9213 Å) and another slightly increased (1.9367 Å), leading to a less distorted octahedron (Figure 8).

The temperature evolutions of the cell parameters, and corresponding unit cell volume, are shown in Figure 6. To compare both lattices, the monoclinic phase parameters have been transformed in the triclinic setting (see Figure 1). With $T$ decreasing from 300 to 50 K, the cell parameters smoothly decrease and at approximately 50 K, the $C2/m$ to $P\bar{1}$ transition occurs with a sharp decrease of $b_t$ and an increase of $a_t$, while $c_t$ increases slightly (not shown) concurrently with an increase of $\beta_t$. The impact of the structural transition on the $Mn^{3+}$ environment is mainly visible on the equatorial Mn−$O_{eq}$ distances, with a clear splitting at the transition of the Mn−$O_{eq}$ distance into a short and a long one (Figure 8), whereas the apical distance Mn−$O_{ap}$ decreases regularly down to 5 K (not shown). Interestingly, the average ⟨Mn−O⟩ distance (2.0356(11) Å) and Jahn−Teller distortion of the $MnO_6$ octahedron do not show any abrupt change at $T_N$, but only a regular decrease with decreasing temperature.

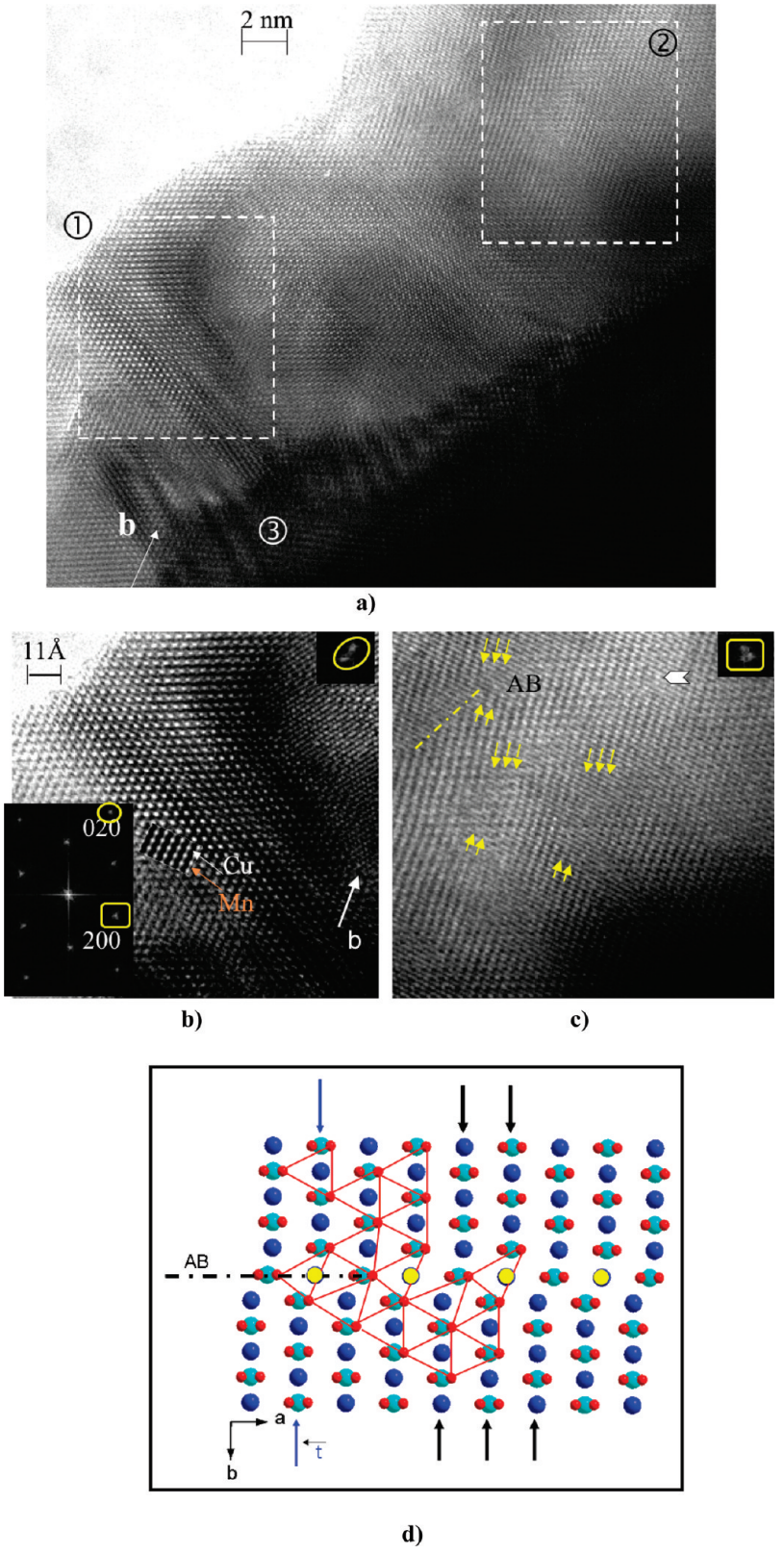


**Figure 5.** (a) Typical [001] HTREM image of a grainy microstructure of the *C2/m* phase characterized by three zones; (b) enlarged image (area 1) of the regular zone with insertion of calculated image; the distortion is observed through the variation of contrast and the enlarged 020 reflection of the FFT in inset; (c) enlarged image of a defective zone (area 2) with the formation of dislocations and antiphase boundaries, the 200 reflection of the corresponding FFT is enlarged; (d) idealized drawing of the bent atomic rows, dislocation and antiphase boundary.

Similarly to the $CuMnO_2$[6] and $NaMnO_2$,[5] the coupling between the magnetic and the structural transitions in $Cu_{1.04}Mn_{0.96}O_2$ allows the lifting of the geometric magnetic frustration inherent to the isosceles triangles array of $Mn^{3+}$ atoms with uniaxial magnetic anisotropy. As previously described, the two longest equal Mn−Mn distances in the monoclinic cell are renormalized in two different Mn−Mn values in the triclinic cell; the sharpness of

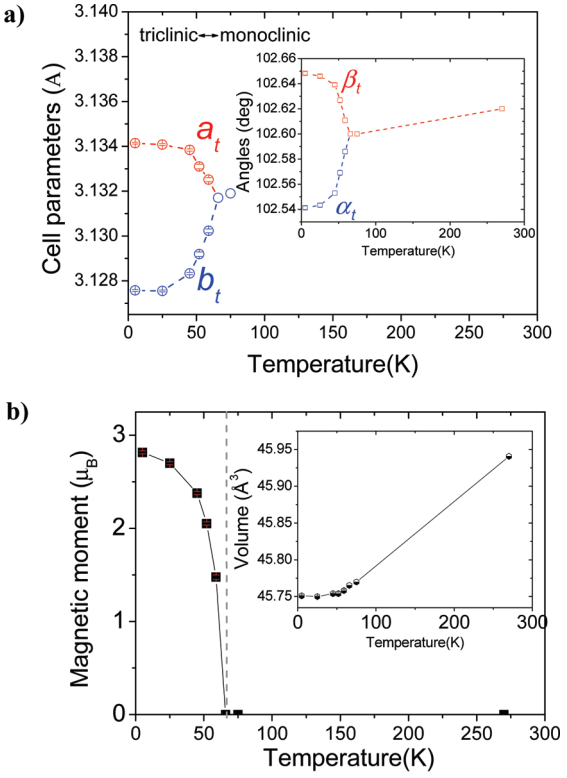


**Figure 6.** From Rietveld refinements of the HRPD neutron powder diffraction data, evolution vs temperature of (a) the $a_t$ and $b_t$ unit cell parameters (in the $P\bar{1}$ space group) with $\alpha_t$ and $\beta_t$ angles in inset and (b) the Mn magnetic moment and cell volume $V$ in the inset.

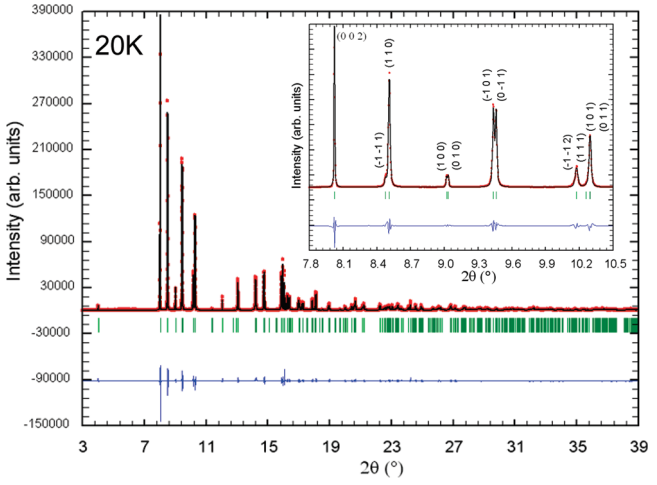


**Figure 7.** Rietveld refinement of the 20 K synchrotron X-ray powder diffraction data of $Cu_{1.04}Mn_{0.96}O_2$. Inset: detail of the refined and experimental profiles.

the transition, corresponding to a larger contraction along $b_t$ than along $a_t$, is shown in Figure 8. The shortest Mn−Mn distance on the contrary decreases regularly with temperature down to 5 K, with no observable abrupt change at $T_N$.

As already mentioned for delafossite-type compounds, the Cu−O distance remains almost unchanged throughout the whole temperature range.[22] In fact, a change in the

(22) Poienar, M.; Damay, F.; Martin, C.; Hardy, V.; Maignan, A.; André, G. *Phys. Rev. B* **2009**, *79*, 014412.

**Table 3. (a) Low Temperature Crystallographic Parameters, Refined from HRPD, and (b) Corresponding Inter Atomic Distances (Å) with Multiplicity and Angles (deg)**

(a) Low Temperature Crystallographic Parameters, Refined from HRPD

| | bank1 | bank2 |
|---|---|---|
| $P\bar{1}$ (no. 2) | | |
| $a_t$ = 3.1341(4) Å | | |
| $b_t$ = 3.1275(4) Å | $R_{Bragg}$ = 3.51% | $R_{Bragg}$ = 2.09% |
| $c_t$ = 5.8935(5) Å | $R_F$ = 3.62% | $R_F$ = 1.96% |
| $\alpha_t$ = 102.54(1)° | $\chi^2$ = 1.68 | $\chi^2$ = 7.62 |
| $\beta_t$ = 102.64(1)° | | |
| $\gamma_t$ = 54.784(4)° | | |
| $V$ = 45.751(1) Å$^3$ | | |

| atom | Wyckoff site | $x$ | $y$ | $z$ | $B_{iso}$ (Å$^2$) |
|---|---|---|---|---|---|
| Cu | (1h) | 0.5 | 0.5 | 0.5 | 0.300(11) |
| Mn,Cu | (1a) | 0 | 0 | 0 | 0.268(15) |
| O | (2i) | 0.405(3) | 0.409(3) | 0.178(5) | 0.262(10) |

(b) Corresponding Inter Atomic Distances (Å) with Multiplicity and Angles (deg)

| | | | |
|---|---|---|---|
| Cu−O | 1.8358(4) (×2) | $O_{eq}$−Mn−$O_{eq}$ | 96.61(6) |
| Mn−$O_{eq}$ | 1.9213(9) (×2) | $O_{ap}$−Mn−$O_{eq}$ | 96.87(10) |
| | | | 96.69(10) |
| Mn−$O_{eq}$ | 1.9367(9) (×2) | Mn−O−Mn | 96.69(4) |
| | | | 96.87(4) |
| | | | 96.61(4) |
| Mn−$O_{ap}$ | 2.2488(14) (×2) | | |
| Mn−Mn | 2.8809(1) | | |
| Mn−Mn | 3.1341(1) | | |
| Mn−Mn | 3.1276(1) | | |

$c$-axis or in the $\beta$-angle does not necessarily have a direct effect upon the Cu−O distance, as displacements of Cu perpendicularly to the O−Cu−O dumbbell or a slight relaxation of the compression of the $MnO_6$ octahedra perpendicularly to the ($a$, $b$) plane are possible.

Before the 3D magnetic ordering, magnetic diffuse scattering becomes clearly observable on the neutron diffraction data from 80 K downward; it increases until the appearance of the antiferromagnetic peaks around 60 K that can be indexed with a propagation vector $\mathbf{k} = (0\ ^1/_2\ 0)$ in the $P\bar{1}$ unit cell (Figure 9); that is, equivalent to ($^1/_2\ ^1/_2\ 0$) with respect to the C-centered monoclinic unit cell. The spins point roughly along the direction of the $d_{z^2}$ orbitals; they only deviated with ≅ 8° from the Mn−O longest inter atomic distance, as expected from the easy-axis anisotropy for the $Mn^{3+}$ site; the temperature dependence of the magnetic moment of Mn, refined from NPD data, is plotted in Figure 6b. At 5 K the components of the magnetic moment are 1.65(4) $\mu_B$ along $a_t$, 1.41(4) $\mu_B$ along $b_t$, and 1.65(3) $\mu_B$ along $c_t$ axis, which correspond to 2.82(2) $\mu_B$ per site (i.e., for 0.96 $Mn^{3+}$), much lower than the 3.84 $\mu_B$ expected value ($S = 2$ for HS $Mn^{3+}$). Like in $CuMnO_2$, within the ($a$, $b$) plane, the coupling is therefore ferromagnetic along $a_t$ (that is for the longest Mn−Mn distance), and antiferromagnetic along the $b_t$ and [1 $\bar{1}$ 0] directions (the latter corresponding to the shortest Mn−Mn distance). Along the $c_t$-axis, the interplane coupling is ferromagnetic, which is in clear contrast with the antiferromagnetic interplane coupling reported for $CuMnO_2$. As described above, the unit cell parameters of $Cu_{1.04}Mn_{0.96}O_2$ and $CuMnO_2$

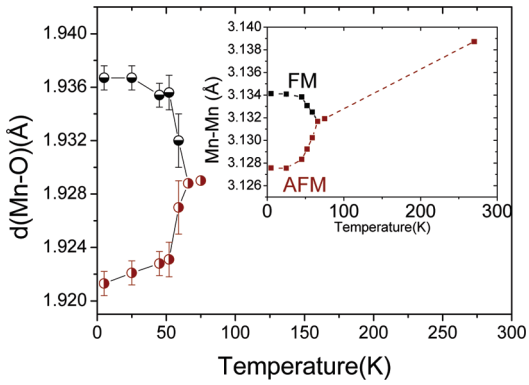


**Figure 8.** Temperature evolution of the Mn−O distances in the (*a*, *b*) plane and, in the inset, of the two longest Mn−Mn distances.

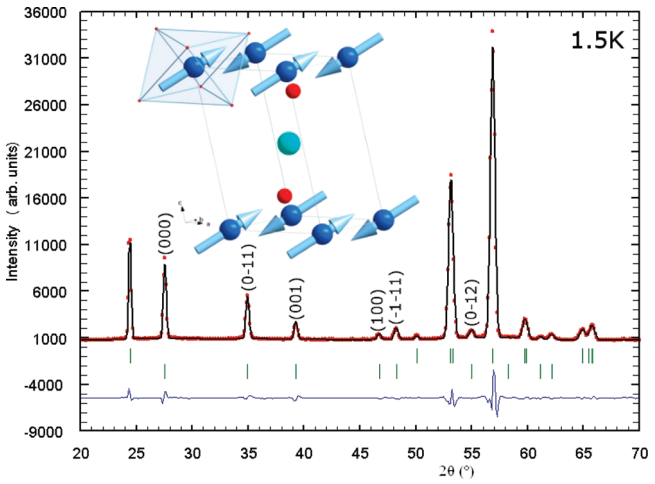


**Figure 9.** Low-angle part of the Rietveld refined neutron powder diffraction data of $Cu_{1.04}Mn_{0.96}O_2$ at 1.5 K (G4.1 diffractometer, $R_{\text{Bragg magnetic}}$ = 5.04%). Magnetic peaks indexation is shown for the propagation vector $\mathbf{k} = (0\ ^1/_2\ 0)$ ($P\bar{1}$ space group). Experimental data are represented by open circles, the calculated profile by a continuous line, and the allowed structural (upper row) and magnetic (lower row) Bragg reflections by vertical marks. The difference between the experimental and calculated profiles is displayed at the bottom of the graph. Inset: Illustration of the corresponding magnetic structure.

follow the same kind of behavior versus *T*, leading nevertheless to a different coupling along *c*.

In term of magnetic exchanges, direct Mn−Mn interactions have to be considered as dominant in-plane but indirect exchanges (via oxygen) could also play a role, all Mn−O−Mn angles being close to 90°. The super-super exchange, along Mn−O−Cu−O−Mn pathways, has also to be taken in consideration to explain the well established 3D magnetic order. In fact super-super exchange via diamagnetic cation is quite common, as discussed in numerous oxides.[23,24] More investigations are required to go further in this discussion because it is first necessary to know the oxidation state of each cation in $CuMnO_2$ and $Cu_{1.04}Mn_{0.96}O_2$.

Note that a second minority magnetic phase with $\mathbf{k} = (^1/_2\ ^1/_2\ 0)$ in $C\bar{1}$ [or $(0\ ^1/_2\ 0)$ in $P\bar{1}$] was also mentioned in ref 6 which can be understood, based on these new data, as resulting from a small amount of $Cu_{1+x}Mn_{1-x}O_2$ in the studied $CuMnO_2$ sample.

## Discussion

In $Cu_{1.04}Mn_{0.96}O_2$, the magnetic transition temperature is slightly higher than the structural transition one (60 K and 50 K, respectively), suggesting a slight difference in the magneto-elastic coupling to release the magnetic frustration, compared to $CuMnO_2$ for which the long-range 3D magnetic ordering occurs simultaneously with the lowering of symmetry of the crystalline structure.[25] In both compounds, $CuMnO_2$ and $Cu_{1.04}Mn_{0.96}O_2$, the magnetic couplings in the (*a*, *b*) plane, that is, in the distorted triangular lattice, are similar, but they differ along the *c* axis: the small substitution of Cu for Mn changes the interlayer coupling from antiferromagnetic to ferromagnetic. This drastic change in the magnetic structure, induced by a very small cationic substitution, shows that a delicate balance exists in the magnetic interactions in competition to stabilize the low temperature ground state. The subtle differences in interatomic distances and angles induce strong modification in magnetic couplings, suggesting thus that these systems are close to instability.

The effect of a small level of substitution in a frustrated triangular lattice is a very challenging issue. For instance, the substitution in $CuFeO_2$ prevents the collinear four-sublattice magnetic structure that is the ground state below $T_{N2} = 11$ K, and stabilizes, like in $CuFe_{1-x}Al_xO_2$,[7−9] an incommensurate magnetic structure. This has been explained considering that substitution disturbs the delicate balance of competing exchange interactions and prevents it as a result the quasi-Ising ordering of $Fe^{3+}$, which retrieves its Heisenberg spin character. It has also been proposed[7−9] that doping with a non-magnetic impurity like $Al^{3+}$ may release the spin frustration without the need for a lattice distortion. It is not the case here for $Cu_{1+x}Mn_{1-x}O_2$, as spins order collinearly with a lattice distortion. Unlike $CuFeO_2$, in which substitution affects principally the balance of the in-plane couplings, in $CuMnO_2$ it modifies the interplane coupling.

Substitution effects on other delafossite compounds have been rather extensively studied, as they are known to strongly modify their physical properties, and in particular their conductivity.[26,27] However, the helicoidal magnetic structure of $CuCrO_2$, characterized by a stacking of planes weakly and ferromagnetically coupled together, is not changed upon substitution.[22,28] The fact that substitution does not modify the magnetic structure of $CuCrO_2$ is likely to result from the very short correlation

(23) Osmond, W. P. *Proc. Phys. Soc.* **1965**, *85*, 1191.
(24) Lee, K.-S.; Koo, H.-J.; Whangbo, M.-H. *Inorg. Chem.* **1999**, *38*, 2199.
(25) Vecchini, C.; Poienar, M.; Damay, F.; Adamopoulos, O.; Daoud-Aladine, A.; Lappas, A.; Perez-Mato, J. M.; Chapon, L. C.; Martin, C. *Phys. Rev. B* **2010**, *82*, 094404.
(26) Okuda, T.; Jufuku, N.; Hidaka, S.; Terada, N. *Phys. Rev. B* **2005**, *72*, 144403.
(27) Nagarajan, R.; Draeseke, A. D.; Sleight, A. W.; Tate, J. *J. Appl. Phys.* **2001**, *89*, 8022.
(28) Poienar, M.; Damay, F.; Martin, C.; Robert, J.; Petit, S. *Phys. Rev. B* **2010**, *81*, 104411.

length along *c* that substitution does not degrade any further.

A similar magnetic structure to $Cu_{1.04}Mn_{0.96}O_2$, with the same propagation vector $\mathbf{k} = (0\ ^1/_2\ 0)$, in a similar triclinic unit cell, has been observed in the case of $NaMnO_2$.[5] The evolution of unit cell and crystallographic parameters reveals close characteristic behavior, namely, lengthening of one of the in-plane Mn−Mn interatomic distances and the contraction of the other one, even though the magnetic behavior is different in the sense that broader diffuse magnetic scattering features are observed in the neutron powder diffraction patterns of $NaMnO_2$.[5] In all these $ABO_2$ compounds, it is probable that, not only the nature of the $BO_2$ sheet, but also the one of the A layer plays a role. For instance, the copper layer is more flexible than the sodium one (because of their different oxygen coordination), and it could have an effect upon the nanostructural state of the compounds. In fact, as explained in the first section of this paper, all the observed defects in $Cu_{1.04}Mn_{0.96}O_2$ break the long-range 2D character of the crednerite structure, and thus may promote 3D magnetic ordering. Nevertheless, to know if there is a clear correlation between strain parameters (refined from NPD and X-ray synchrotron data), defects observed by TEM and long and short-range magnetic ordering, it should be necessary to perform the same kind of systematic study on $CuMnO_2$ and $NaMnO_2$.

## Conclusion

In conclusion, the synchrotron and neutron powder diffraction study of $Cu_{1.04}Mn_{0.96}O_2$ shows that the partial Cu for Mn substitution affects mainly the sign of the interplane magnetic coupling (between two $MnO_2$ layers) that changes from antiferromagnetic in $CuMnO_2$ to ferromagnetic in $Cu_{1.04}Mn_{0.96}O_2$. In both compounds, frustration is lifted through a magneto-elastic symmetry lowering of the triangular lattice leading to identical in-plane magnetic orderings in $Cu_{1.04}Mn_{0.96}O_2$ and $CuMnO_2$. In addition, the highly perturbed nanostructural state of $Cu_{1.04}Mn_{0.96}O_2$, observed by electron microscopy, explains the strain parameters necessary to refine the neutron and X-ray diffraction patterns and is proposed to play a role in the magnetic behavior.

**Acknowledgment.** Financial support was partly provided by the French Agence Nationale de la Recherche (ANR-08-BLAN-0005-01). A.L. acknowledges partial support from the European Commission ("Construction of New Infrastructures", ISIS Target Station II, contract no. 011723), and the EU access to research infrastructures program of ISIS (Project Reference: HPRI-CT-2001-00116).